XIN LI[1], MENG WANG[1], HAN QI[2], JIE LI[3*], CHANGCHUN PAN[4],
JING ZHANG[3], JINGMAN LAI[3]

LOW TEMPERATURE WELDING TEST AND NUMERICAL SIMULATION OF METALLURGICAL PHASE TRANSFORMATION OF Q460GJC THICK PLATE

This paper conducts low temperature welding tests on Q460GJC thick plate (60 mm), and based on the basic theory of phase transformation structure evolution, a three-dimensional microstructure evolution analysis method for large welded joints is established, and the analysis of the evolution process of multi-layer and multi-pass weld structure under the low temperature environment of thick plates is completed. The comparison and analysis of test and numerical simulation results are in good agreement, which proves that the welding phase transformation model realizes the digitalization of metallurgical phase transformation in steel structure welding, and optimizes welding process parameters. It is of great significance to improve the quality of welding products and lay a foundation for predicting the performance of welded joints from the micro level.

Keywords: Low temperature welding of thick plate; Q460GJC; Microstructure; Numerical simulation of phase transition

1. Introduction

In winter, the welding of steel structure nodes under outdoor low temperature environment is easy to cause cold crack or brittle fracture in the later stage due to unreasonable temperature control [1], which greatly increases the difficulty of qualified welding quality. According to GB 50661-2011 "Welding Code for Steel Structure" [2], the welding environment temperature should be lower than –10°C, and the test results are partly affected by the uncertain factors such as welder level and welding environment control [3], which may interfere with the formulation of the process scheme. Welding process simulation can be through quantitative physical model to simulate the whole welding process, using physical information and process parameters, and carried out on the computer welding design and process simulation, the whole process of 3d characterization, quantitative analysis of plate low temperature welding joint performance, clarify the key points of plate low temperature welding quality control, and improve the low temperature welding parameters proposed scientific and welding process efficiency.

In order to quantitatively reflect the microstructure transformation of the thermal influence area of the welding process, this paper carries out low temperature welding test with 60 mm thick Q460GJC steel plate welding joints to obtain the temperature distribution and microstructure of the welding joints of the welding process, laying a foundation for the prediction and guiding the development of the welding process scheme.

2. Theory of foundations

2.1. Double-ellipsoidal heat source model

The simulation of the arc welding heat source often adopts the double ellipsoid (DE) heat source model, which was proposed by Goldak et al. [4] in 1984. It believes that the heat source power density of the welding arc heating spots is distributed in the double ellipsoid moving heat source model. The DE model divides the body heat source into two front and back parts, which can better simulate the different temperature gradient [5] of the front and back end of the moving heat source during the welding process. The heat flow density is normally distributed by Gaussian function in the semi-ellipsoid, and the maximum value is in the central part, and decreases exponentially from the center to the edge.

1   BEIJING CONSTRUCTION ENGINEERING GROUP CO., LTD, BEIJING, 100032, P.R. CHINA
2   BEIJING THIRD CONSTRUCTION ENGINEERING CO., LTD, BEIJING, 100032, P.R. CHINA
3   CENTRAL RESEARCH INSTITUTE OF BUILDING AND CONSTRUCTION CO., LTD. MCC, BEIJING, 100032, P.R. CHINA
4   CHINA STATE SHIPBUILDING INTERNATIONAL ENGINEERING CO., LTD. CSIE, BEIJING, 100000, P.R. CHINA

*   Corresponding author: 326618260@qq.com

1534

The expression of heat source distribution in the ellipsoid of the first half is:

$$q(x, y, z) = \frac{6\sqrt{3}f_1 Q}{\pi a_1 bc\sqrt{\pi}} \exp\left(-3\frac{x^2}{a_1^2}\right)$$
$$\exp\left(-3\frac{y^2}{b^2}\right)\exp\left(-3\frac{z^2}{c^2}\right) \quad (1)$$

The expression of heat source distribution in the second half of the ellipsoid is:

$$q(x, y, z) = \frac{6\sqrt{3}f_2 Q}{\pi a_2 bc\sqrt{\pi}} \exp\left(-3\frac{x^2}{a_2^2}\right)$$
$$\exp\left(-3\frac{y^2}{b^2}\right)\exp\left(-3\frac{z^2}{c^2}\right) \quad (2)$$

In the formula: $q = \eta UI$, η – efficiency of heat source, U – welding voltage, I – welding current; a_1, a_2, b, c – Elliptic shape parameters; f_1, f_2 – front and posterior ellipsoidal heat distribution function, $f_1 + f_2 = 2$.

2.2. Governing equation

Welding heat conduction is a typical nonlinear transient problem [6]. For a homogeneous and isotropic continuum medium, the control equation based on energy conservation is obtained as follows:

$$\frac{\partial T}{\partial t} = \frac{\lambda}{c\rho}\left(\frac{\partial^2 T}{\partial x^2} + \frac{\partial^2 T}{\partial y^2} + \frac{\partial^2 T}{\partial z^2}\right) + \frac{1}{c\rho}\frac{\partial Q_v}{\partial t} \quad (3)$$

In the formula: T – temperature; ρ – density; c – specific heat capacity; λ – thermal conductivity; Q_v – overflow of the dissipated heat energy per unit volume; $\frac{\partial Q_v}{\partial t}$ – internal heat source strength, W/m³.

2.3. Heat Conduction Boundary Conditions

Welding physical process usually includes the generation and transmission of welding heat, the flow and solidification of weld pool, micro-structure evolution of materials, welding stress and deformation, involving temperature field, stress field, tissue field and molten pool flow field. Although numerical simulation techniques and high-performance computers have been rapidly developed and widely used, it is very difficult to simulate all the physical processes involved in welding simultaneously [7]. This paper focuses on the welding tissue evolution and ignores the influence of the welding mechanical process and the welding flow process on the welding tissue evolution.

In the process of welding heat conduction, the temperature of the weld changes sharply with the movement of the heat source, so there is a sharply changing temperature gradient inside the solder. According to the heat transfer theory, the heat transfer process includes three basic heat transfer forms: heat conduction, heat transfer and radiation heat transfer [8]:

(1) Heat conduction can be expressed by the Fourier's law:

$$q^* = -\lambda\frac{\partial T}{\partial n} \quad (4)$$

In the formula: λ – thermal conductivity; $\frac{\partial T}{\partial n}$ – temperature gradient.

(2) The law of heat transfer: the heat current density is proportional to the heat transfer coefficient of the convection surface and the difference between the solid surface temperature and the temperature of the gas or liquid.

$$q_c^* = \alpha_c(T - T_0) \quad (5)$$

In the formula: α_c – coefficients of the convection-flow surface heat transfer; T – solid surface temperature; T_0 – gas or liquid temperature.

(3) Radiation heat transfer law: the heat loss caused by thermal radiation calculated by the Stephen-Boltzmann law can be calculated according to the following formula:

$$q_r^* = \varepsilon C_0(T^4 - T_0^4) \quad (6)$$

In the formula: ε – Darkness coefficient, $\varepsilon < 1$, for rough and oxidized steel surfaces, $\varepsilon = 0.6 \sim 0.9$; C_0 – The Stephen-Boltzmann constant, $C_0 = 5.67\times10^{-14}$ J/(mm²·s·K⁴); T – object temperature, T_0 – ambient temperature.

2.4. The theoretical model of phase transition

2.4.1. Characteristic point temperature of the phase transition

For the welding process, the phase transition characteristic temperature should be determined by the corresponding CCT graph [9], including liquid phase line temperature T_l, solid phase line temperature T_s, ferrite start dissolution temperature above the eutectoid line T_F, austenitic temperature A_{e3}, pearlite phase transition temperature A_{e1}, bainite phase transition temperature B_s, and Martensite phase transition temperature M_s. These characteristic point temperatures can be determined by:

$$T_1 = 1530.0 - 80.531 w_c \quad (7)$$

$$T_s = \frac{B}{A - \lg\left(C_m^a C_0^b\right)} \quad (8)$$

$$A_{e3} = 912 - 203\sqrt{w_c} - 15.2w_{Ni} + 44.7w_{si} +$$
$$+ 104w_v + 31.5w_s + 13.1w_w - 30w_{Mn} - 11w_{cr}$$
$$- 20w_{cu} + 700w_p + 400w_N + 120w_{As} + 400w_{Ti} \quad (9)$$

$$A_{e1} = 723 - 10.7w_{Mn} - 16.9w_{Ni} - 29w_{Si}$$
$$+ 16.9w_c + 290w_s + 64w_{wi} \quad (10)$$

$$B_s = 656 - 58w_c - 35w_{Mn} - 75w_{Si}$$
$$- 15w_{Ni} - 34w_c - 41w_{s0} \quad (11)$$

$$M_s = 561 - 474w_c - 33w_{yn} - 17w_{Ni}$$
$$- 17w_{cr} - 21w_{M0} \quad (12)$$

In the formula: w_c – carbon content in steel (mass fraction /%), the remaining element symbols also represent their content; A, B, a and b are constants, respectively take 3.11, 7520.0, 1.0 and 1.0, C_m^a and C_0^b are respectively the metallic and nonmetallic contents in the sediments (mass fraction /%).

2.4.2. The Phase Transition Model

The welding metallurgical phase transition model mainly includes diffusion phase transition of ferrite, pearlite and bainite and non-diffusion phase transition of martensite.

At present, there are mainly three numerical calculation models for the diffusive phase transition: first, the phase transition thermodynamics and phase transition dynamics at any time as discussed [10]; second, based on the Avrami equation, Using the isothermal transition phase diagram (TTT) and simultaneously using the Scheil additivity principle to calculate the phase transition during cooling. To address the potential severe bias of the additivity principle during the initial period of calculation, the continuous cooling tissue transition diagram (SH-CCT) was used to determine the start time of the phase transition [11]; third, directly using the SH-CCT diagram to calculate the phase transition, the calculation of the phase transition via the mathematical model established by the SH-CCT plot and the deformation formula of the Avrami equation were successfully achieved [12].

For the non-diffusion-type phase transition, the relatively simple Koistinen-Marburger phase transition model [13] is usually used for numerical simulation calculation.

(1) Speed formula of austenitic grain growth during heating process:

$$\frac{dg}{dt} = \frac{1}{2g} k \left[\exp\left(-\frac{Q}{RT}\right) \right] \quad (13)$$

In the formula: g – grain size, μm; k – grain growth constant, related to the steel composition and temperature changes, $k = 7 \times 10^{11}$ μm²/s; Q – grain growth and activation energy, $Q = 241$ kJ/mol.

(2) The reaction velocity formula of austenite decomposition during continuous cooling based on Kirkaldy phase transition model [14]:

$$\frac{dX}{dt} = B(G,T)X^m(1-X)^p \quad (14)$$

In the formula: X – volume fraction of the transition products; B – efficient coefficient; G – austenite grain size; m, p – the semi-empirical coefficients used to ensure the convergence properties, both of which are less than 1.

(3) Speed formula for the decomposition of austenite into ferrite reaction during continuous cooling:

$$\frac{dX}{dt} = \frac{2^{(G-1)/2}\Delta T^2 DX^{2(1-x)/3}(1-X)^{2X/3}}{59.6w_{Mn} + 1.45w_{Ni} + 67.7w_{Cr} + 24.4w_{Mn})}$$
$$\cdot \exp(-23000/RT) \quad (15)$$

In the formula: G – ASTM austenite grain size; ΔT – degree of super-cooling, $\Delta T = A_{e3} - T$; X – ferrite volume fraction, $X = X_F/X_{FE}$, X_F and X_{FE} are the ferrite content when formed and balanced, respectively; R – universal gas constant, $R = 8.31$.

(4) Speed formula for the decomposition of austenite into pearlite reaction during continuous cooling:

$$\frac{dX}{dt} = \frac{2^{(G-1)/2}\Delta T^2 DX^{2(1-x)/3}(1-X)^{2X/3}}{5.42(w_{Mn} + 4w_{MoNi} + w_{Cr}) + 1.79} \quad (16)$$

In the formula: $\Delta T = A_{e1} - T$; X – pearlite volume fraction, $X = X_P/X_{PE}$, X_P and X_{PE} are the pearlite content when formed and balanced, respectively; D – diffusion parameter, which can be calculated by the following formula:

$$\frac{1}{D} = \frac{1}{\exp(-27500/RT)} + \frac{0.01w_c + 0.52w_{Mo}}{\exp(-37000/RT)} \quad (17)$$

In the formula: R – universal gas constant, $R = 8.31$;

(5) Speed formula for the decomposition of austenite into bainite reaction during continuous cooling:

$$\frac{dX}{dt} = \frac{2^{(G-1)/2}\Delta T^2 X^{2(1-x)/3}(1-X)^{2X/3}}{(2.34 + 10.1w_C + 3.8w_{Cr} + 19w_{Mo})f(X,C_i)}$$
$$\cdot \exp(-27500/RT) \quad (18)$$

In the formula: $\Delta T = B_s - T$; X – bainite volume fraction, $X = X_B/X_{BE}$, X_B and X_{BE} are the bainite content when formed and balanced, respectively; $f = (X, C_i)$ can be calculated by the following equation:

$$f(X,Ci) = \exp\left[\begin{array}{c} X^2(1.9w_c + 2.5w_{Mn} + 0.9w_{Ni} \\ + 1.7w_{Cr} + 4w_{N0} - 2.6 \end{array}\right] \quad (19)$$

When the index is negative, $f(X, C_i) = 1$.

(6) The Koistinen-Marburger phase transition model equation used for autenite transition to martensite is expressed as:

$$\theta_M = 1 - \exp\left[-\alpha(M_s - T)\right] \quad (20)$$

In the formula: θ_m – martensite volume fraction, M_s – martensite phase transition temperature (unit: K); α – martensite transition rate associated with the material, which can be calculated as follows in the following equation (21):

$$\alpha = \frac{4.61}{91.7w_c + 161} \quad (21)$$

In the formula: w_c – carbon content in steel (mass fraction /%).

1536

3. Finite Element Model

3.1. Model Building

Establish a thick steel plate Q460GJC geometric model with a size of 800 mm × 508 mm × 60 mm according to the low temperature welding test piece, select 3D 8-node hexahedral solid unit in Simufact Welding post-processing program, adopt transition mesh, close to the weld area mesh and coarse away from the weld area, take 3 mm for weld mesh and 8 mm~15 mm for base material mesh. In Fig. 1, The geometric model (Fig. 1(a)), distribution of the weld pass (Fig. 1(b)), overall model mesh (Fig. 1(c)) and weld mesh (Fig. 1(d)) were consistent with the test plate welding test process.

Each weld pass analysis includes heating, cooling steps and set the residence time between each pass, analysis automatically select the time step, heat conduction analysis, heat load through the double ellipsoid power density distribution heat source [15], output results data including node temperature and the characterization of ferrite, pearlite and bainite of three major state variables.

3.2. Welding Parameter

The plate butt joint welding specimen adopts unilateral V-shaped groove, with an angle of 35° and a bottom width of 8 mm. The base material steel number is Q460GJC-Z25, with a plate thickness of 60 mm. The welding process parameters are shown in TABLE 1: the welding test was carried out in a low temperature environment, taking FCAW-G welding process, using $\Phi1.2$ mm SH.Y81Ni1 (T554T1-1C1A-N2) welding wire, with V-shaped groove. The welding sequence diagram is shown in Fig. 2. It shows 10 layers and 43 passes in the weld, with 8 mm gap and 2 mm blunt edge at the bottom of the weld.
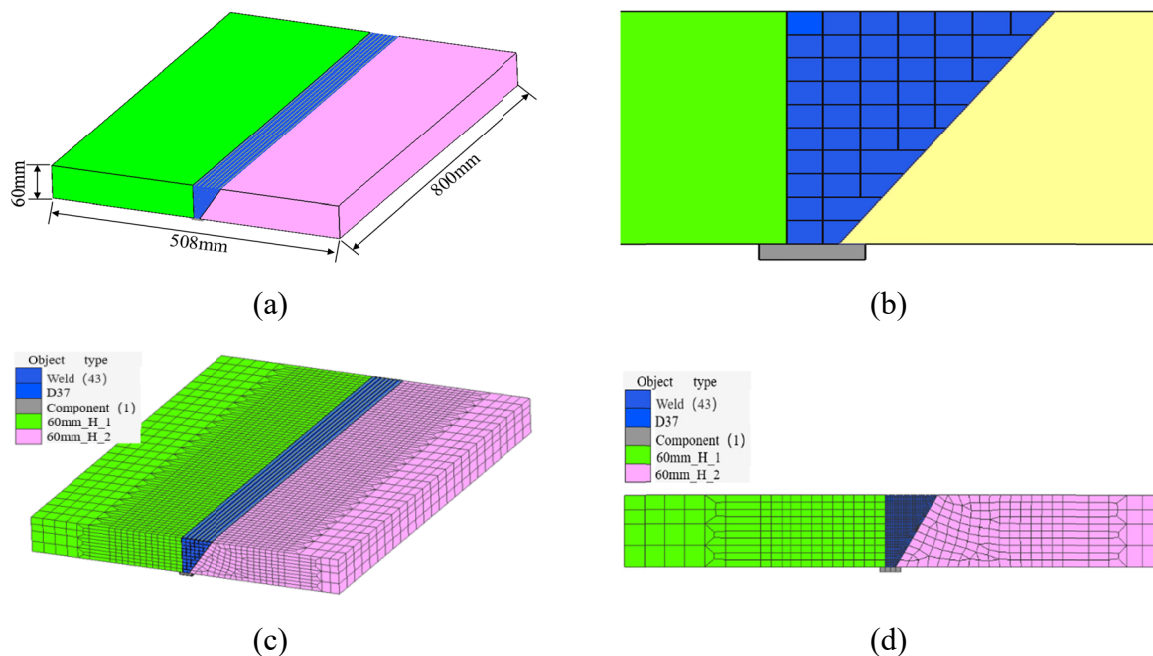

(a)

(b)

(c)

(d)

Fig. 1. Finite element model establishment: (a) Geometric model, (b) distribution of the weld pass, (c) overall model mesh, (d) weld mesh

TABLE 1

Welding test scheme

Welding process	Base material steel number	Standard (mm)	Welding material	Welding specifications (mm)	Welding position	Test condition
FCAW-G	Q460GJC-Z25	60	SH.Y81Ni1 (T554T1-1C1A-N2)	$\Phi1.2$	V	Low temperature

TABLE 2

Welding process parameters

Welding position	Weld pearlite	Welding parameters			
		Welding current (A)	Welding voltage (V)	Speed of welding (cm/min)	Heat input (KJ/cm)
V	Bottoming	160~220	22~29	25~30	7~15
	Filling	200~270	24~31	30~40	7~17
	Facing	200~240	24~28	30~40	7~14

Note: The CO_2 gas flow rate at low temperature is about 20 ±5 L/min.
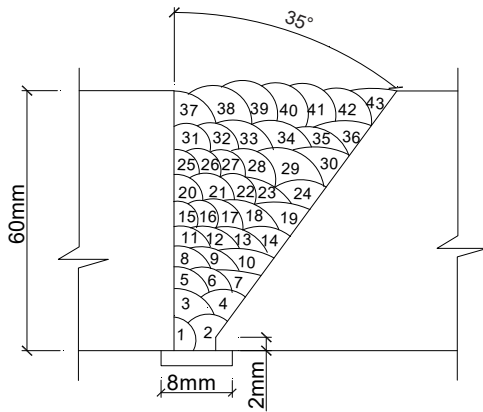
Fig. 2. Schematic diagram of the welding sequence

The welding process parameters are shown in TABLE 2. It contains welding current and welding voltage in different layers according to previous experience, and the speed of welding takes about 30 cm/min, adopting CO_2 as shielding gas.

4. Analysis of The Finite Element and Test Results

### 4.1. Temperature Field Analysis of The Welding Process

First, low temperature welding test is carried out for 60 mm plate. Fig. 3(a) shows the distribution map of temperature measurement points of test plate with 12 measuring points, 5 measuring points on both sides of 15 cm, and 2 measuring points in the middle of plate thickness, numbered as measuring point 11 and 12. Due to the drastic temperature change in the near weld area, the twelve measurement points for temperature analysis at 10 cm to the fusion line were used to compare with the calculation results of the finite element model at the above measurement points to verify the reliability of the model [16]. The temperature of each measurement point shall be measured once and recorded respectively. Each measurement shall be completed as soon as possible after the welding is stopped to ensure the validity of the temperature data. Temperature measurements are shown in

Fig. 3(b), where $t1\sim t6$ successively indicate after preheating, welding after layer 3, layer 6, layer 9, 5 min and 10 min after welding. The temperature measurements for the six series all show a trend of rising first and then falling, and reach a maximum at t4, while each spread value reaches the maximum. The temperature at each point does not exceed 200°C, and the change is relatively gentle, which is conducive to obtaining relatively accurate measurement values and facilitating comparison with the finite element calculation results at the corresponding position.

Second, the calculation of welding temperature field is the basis of the phase transition calculation, the distribution of temperature field directly determines the distribution of phase transition structure [17]. The temperature change of the overall model welding process can be accurately obtained through the Simufact Welding post-processing procedure. The temperature field model of the 60 mm plate docking joint was analyzed by that software. Low temperature is –15°C, with 10 layers and 43 welding passes in the weld. When the specimen is not welded, an initial preheating temperature of 120°C is applied, and the specimen temperature is uniform. Along with the temperature field of the specimen changing gradually in the welding process, the temperature cloud map was intercepted at several different moments from the beginning or end of each welding track, as well as 30 s, 3 min and 6 min post-welding cooling, as shown separately in Fig. 4(a)~(o), showing the complexity of the physical change process of temperature in the multi-layer welding weld area.

According to Fig. 5, the overall model welding starts after preheating to 120°C. Because the welding position is close to the left side of the test plate, the temperature increases rapidly, while the temperature at the slope mouth side decreases first and then increases, and the growth is slower [18].

For the temperature field calculation, since the model in this paper does not consider the physical process of converting the weld from a solid state to a liquid state [19], the region above 1538°C is defined as the melting pool, while the temperature interval of the thermal influence zone is 720°C to 1538°C. Fig. 6(a) is a cloud map of the temperature distribution of the mobile heat source. As you can see, the weld pool area above
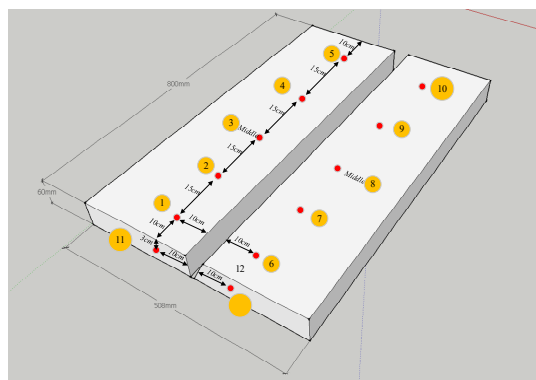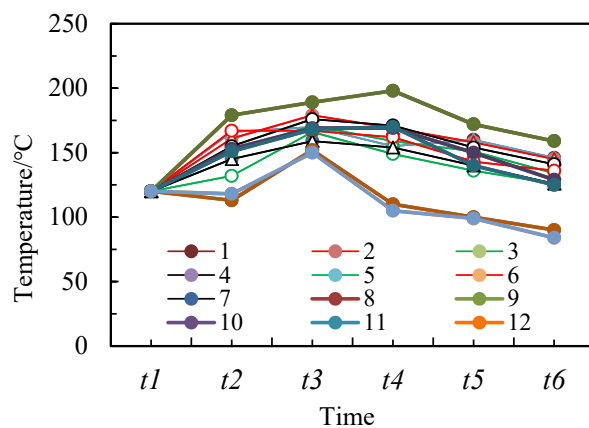
(a)   (b)

Fig. 3. (a) Distribution diagram and (b) temperature curve of measurement points in low temperature welding test
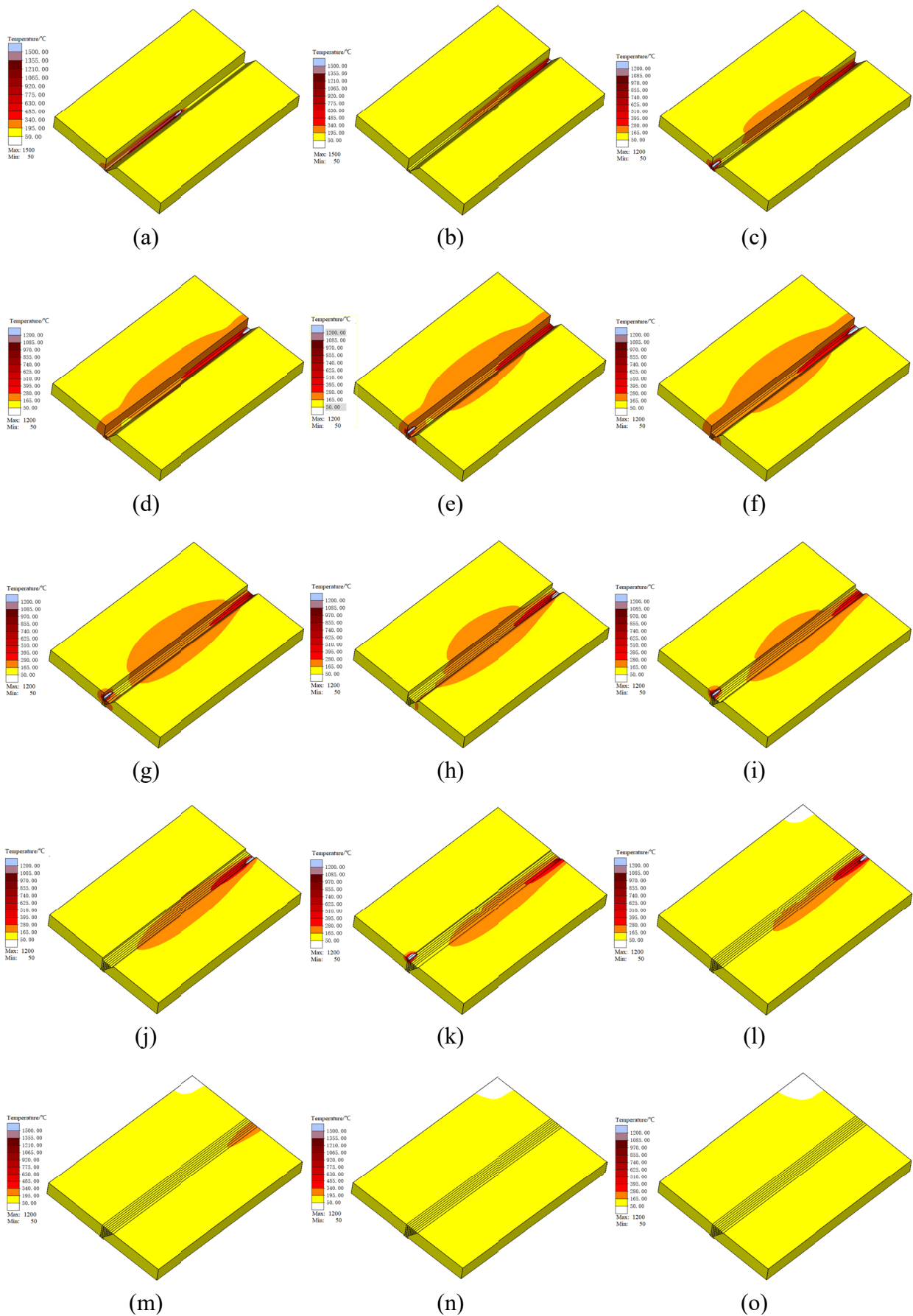
1538

Fig. 4. Overall model welding temperature field: (a) weld base, (b) the end of layer 1 welding, (c) the start of layer 2 welding, (d) the end of layer 2 welding, (e) the start of layer 4 welding, (f) the end of layer 4 welding, (g) the start of layer 6 welding, (h) the end of layer 6 welding, (i) the start of layer 8 welding, (j) the end of layer 8 welding, (k) the start of layer 10 welding, (l) the end of layer 10 welding, (m) 30 s post-welding, (n) 3 min post-welding, (o) 6 min post-welding
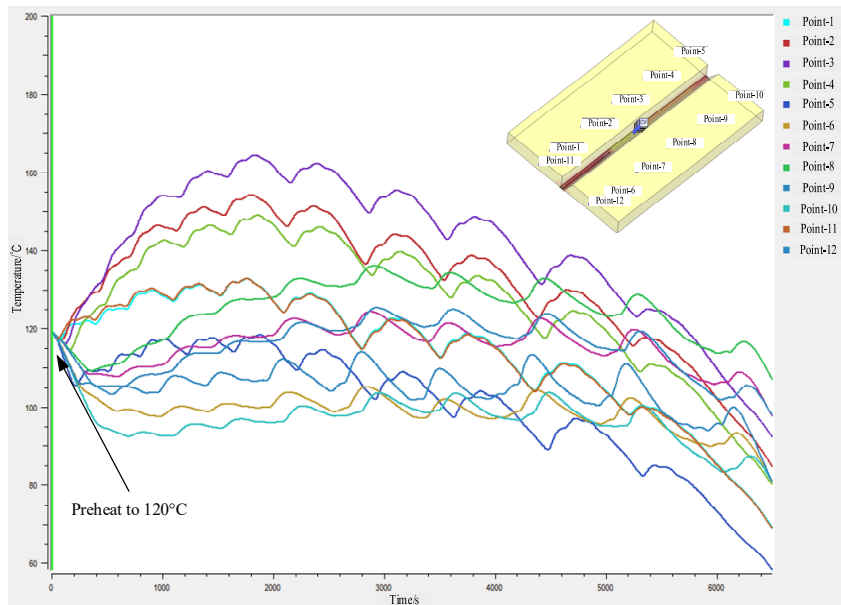
Fig. 5. Numerical simulation of the measurement point temperature change calculation results

1538℃ is roughly the same area as the actual swing welding area, which can accurately simulate the temperature distribution during the movement of the weld pool. The overall model peak temperature cloud map is shown in Fig. 6(b).

Comparing the peak temperature distribution of the weld section in Fig. 7(a) and the macro morphology of the welded joint in Fig. 7(b), it shows that the size of the simulated weld pool and the thermal influence area agrees well with the actual welded

(a)

(b)
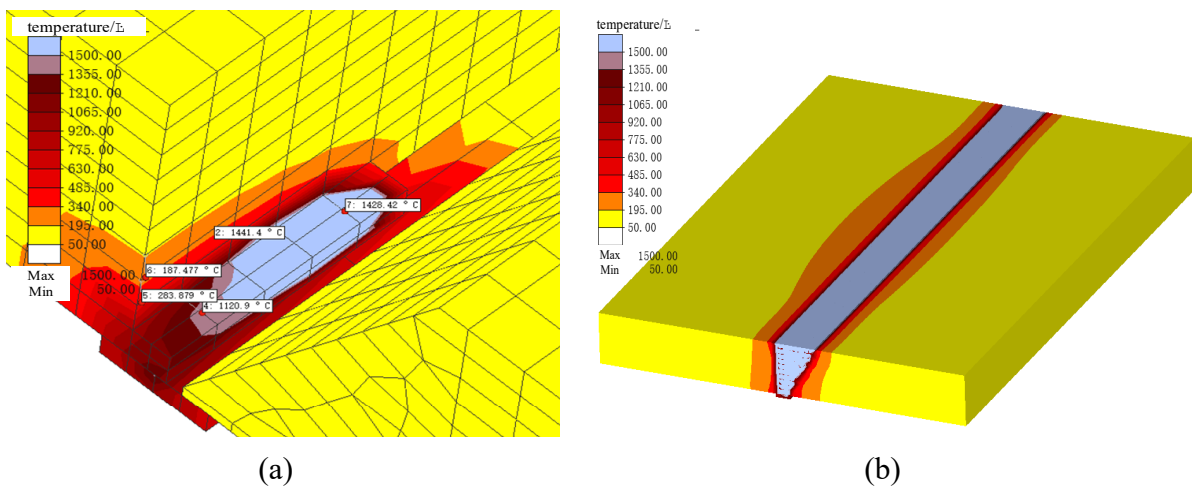
Fig. 6. Temperature cloud map of (a) mobile heat source and the overall docking joint

(a) Peak temperature distribution

(b) Macroscopic topography
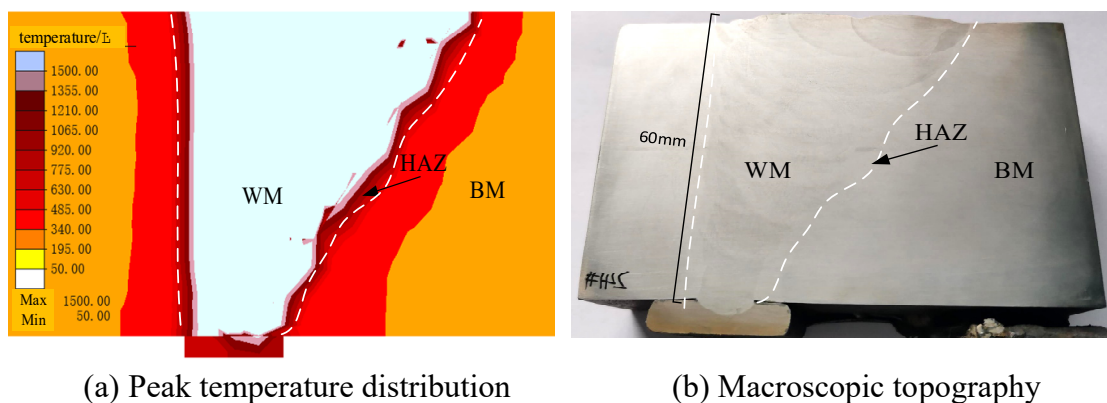
Fig. 7. Peak temperature distribution and macroscopic topography of the weld cross section

1540

joint, which proves that the numerical simulation of welding has high accuracy.

Fig. 8 for the temperature calculation results of each layer, visible each node position has experienced multiple thermal cycle, directly illustrates the complexity of the physical change of thick plate multilayer welding temperature, after analysis it can be found that before the upper layer between the welding temperature is less than 250℃, and the joint performance meets the requirements. Since the metal vaporization process is not considered in this model, the temperature will continue to increase after reaching the vaporization temperature [20], and this maximum temperature exhibited 1538℃ instantly is not of reference significance.

Fig. 9 shows the $t_{8/5}$ cooling rate of weld. It can be seen that the process of multi-layer welding temperature change is very complicated, and the cooling rate of position 1 and 3 at both ends of the weld is higher than that of the middle position 2, and the cooling rate of the weld surface at the same position is higher than that of the center layer [21]. Due to that the larger thermal radiation area at both ends, the thermal conductivity efficiency is higher than that of the middle, and the heat loss is faster. Meanwhile, there was larger cooling rate within the fusion line in comparison to the center line of welded joint in location 1 to 3, due to that the temperature difference within the fusion line is larger, and the heat transfer efficiency is higher.
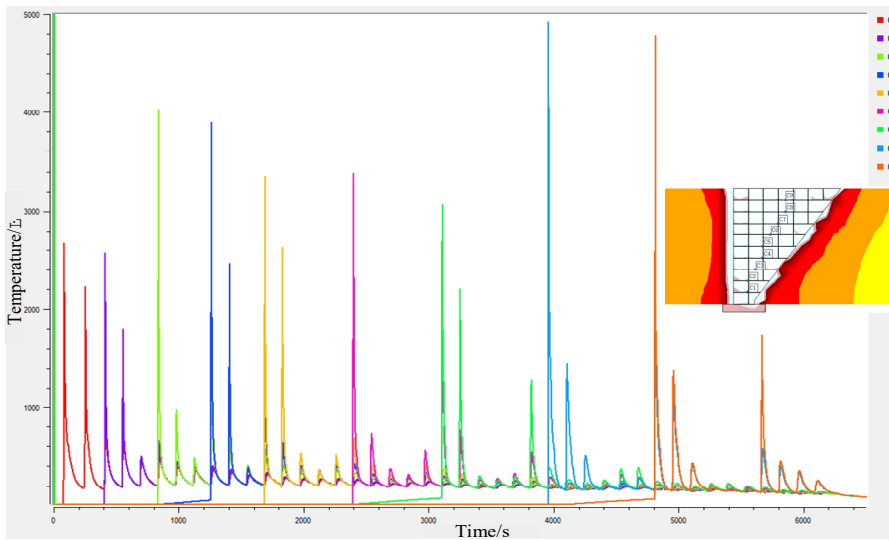

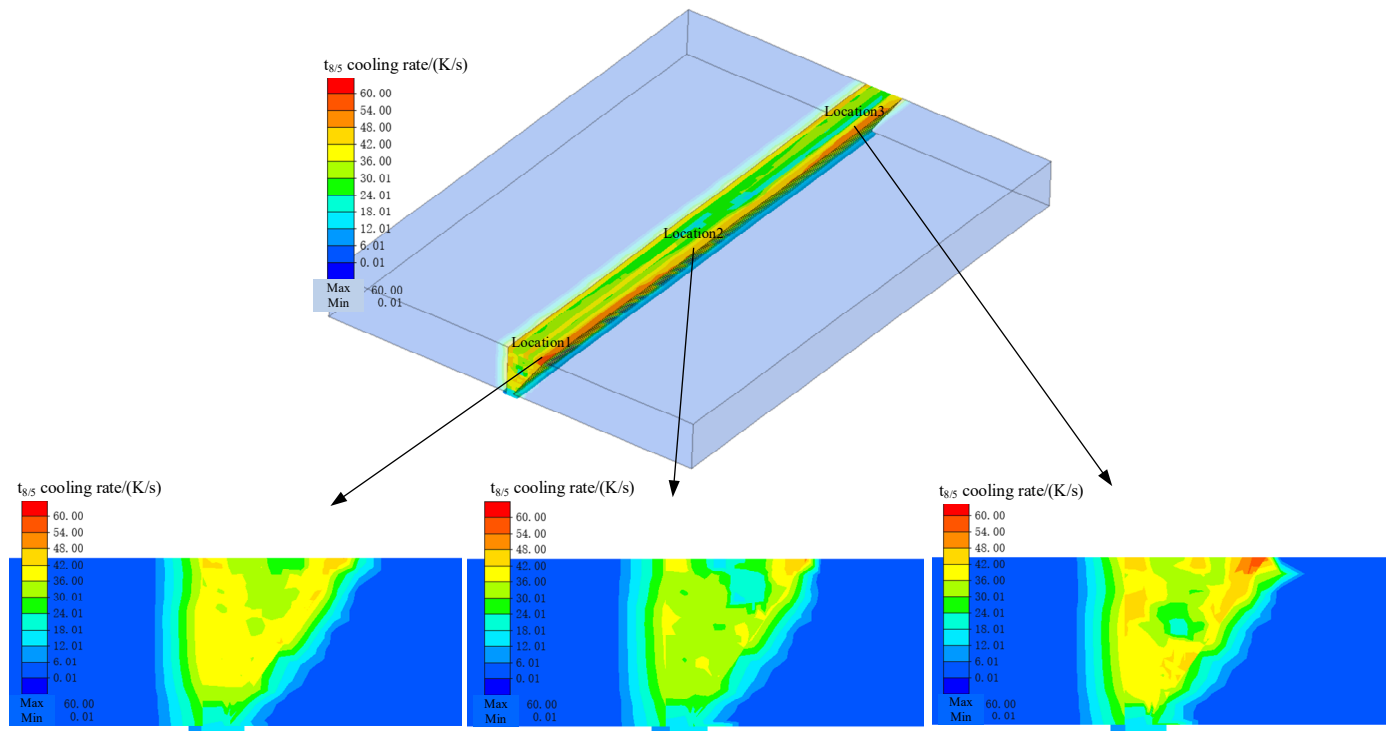Fig. 8. Time curve of each weld temperature

Fig. 9. $t_{8/5}$ cooling rate of cross-section at different positions

4.2. Analysis of The Welding Phase Transition Cloud Diagram

According to the FEM results, Fig. 10 reflects the distribution of ferrite in the welded joint. It can be seen that most of the weld tissue is composed of ferrite, and the ferrite volume fraction at both ends of the weld pearlite in position 1 and 3 is significantly lower than that of the middle part of the weld, due to that the $t_{8/5}$ cooling rate [22]. According to Fig. 9, the $t_{8/5}$ cooling rate at both ends is higher than that of the middle part. For the distribution of ferrite on the weld surface at the same position, the ferrite volume fraction at the groove edge near the parent material is lower than that at the center of the groove, due to that the cooling rate of the groove edge is higher than the rate of the groove center either.

The calculation results of Fig. 11 reflect the distribution of pearlite in the welded joint. It can be seen that the content of pearlite is significantly lower than that of ferrite, and the distribu-
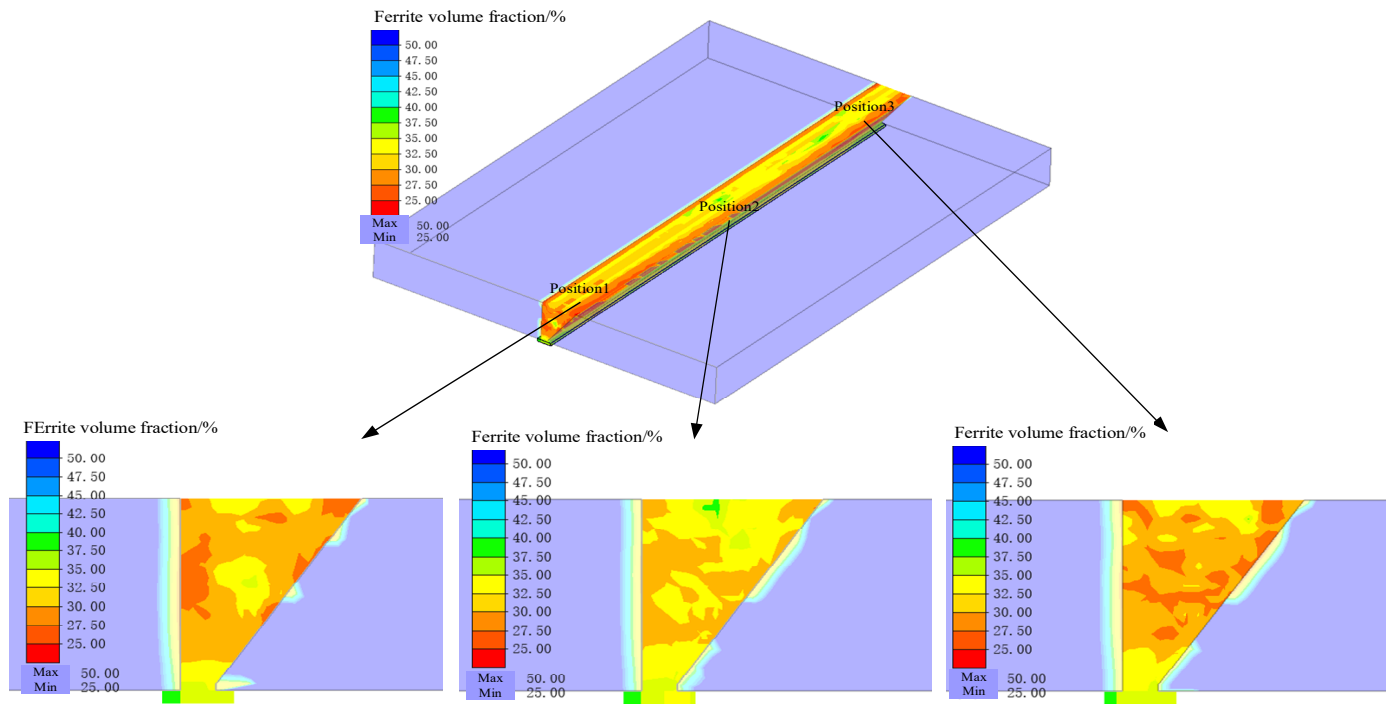

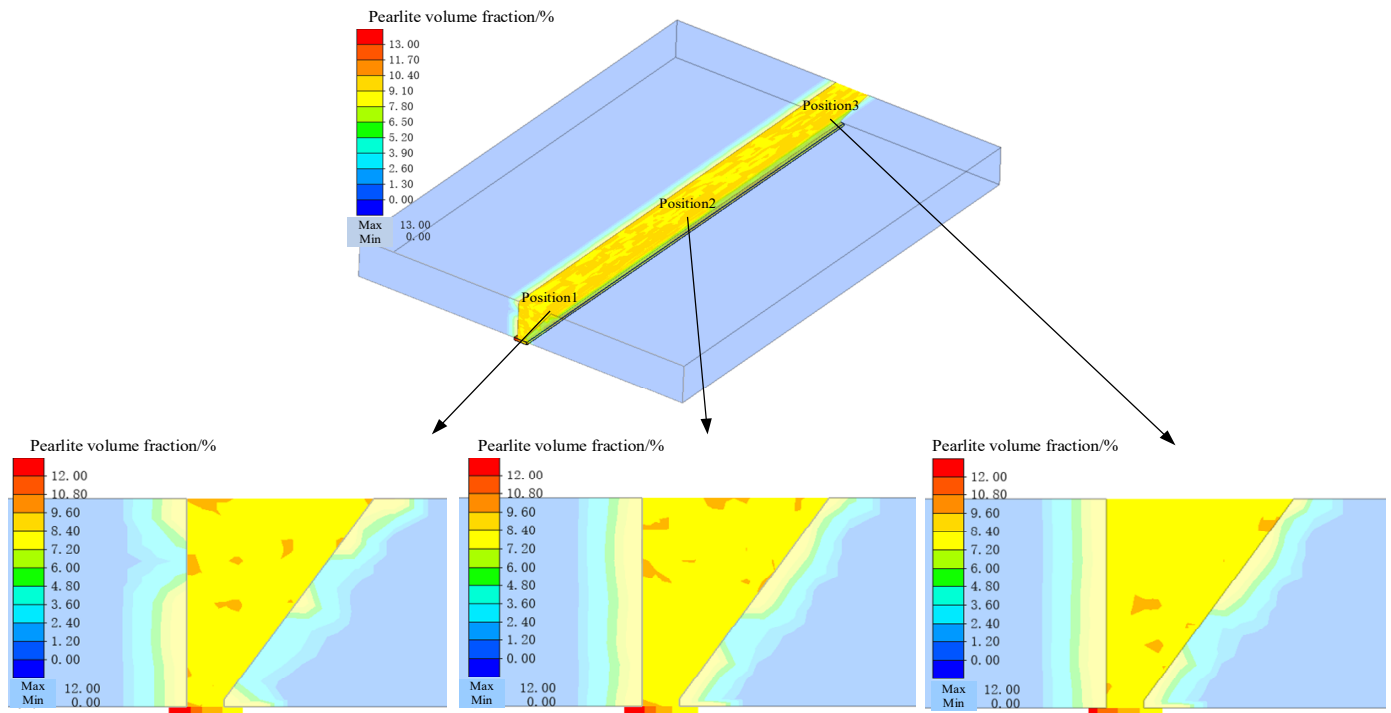Fig. 10. Ferrite volume fraction at different positions

Fig. 11. Pearlite volume fraction at different positions of the weld

tion range in the thermal influence area of the weld is wider than that of ferrite, which also indicates that the temperature range of pearlite is lower than that of ferrite. Due to the $t_{8/5}$ cooling rate within the fusion line is higher than that of the welding passes, there was lower pearlite volume fraction within the fusion line in comparison to the center line of multi-layer welded joint [23].

Fig. 12 shows the distribution of bainite in the welded joint. It can be seen that the content of bainite is also significantly lower than that of ferrite but higher than that of pearlite. The distribution range in the thermal affected area of weld is similar to that of pearlite, and shows a similar pattern to the volume fraction of ferrite [24].

Fig. 13 shows the microstructure observation diagram of weld. According to the test results, the HAZ is mainly the lath-

shaped ferrite growing inward along the original austenite grain boundary and the bainite and granular bainite microstructure with discontinuous distribution between strips composed of carbide. From the calculation results, the maximum location of ferrite and bainite tissue volume fraction is in the thermal influence region.

5. Conclusion

(1) The Goldak double ellipsoid power density distribution heat source model is adopted in the welding of 60 mm thick Q460GJC steel plate under –15°C low temperature condition, meanwhile using the professional analysis soft-
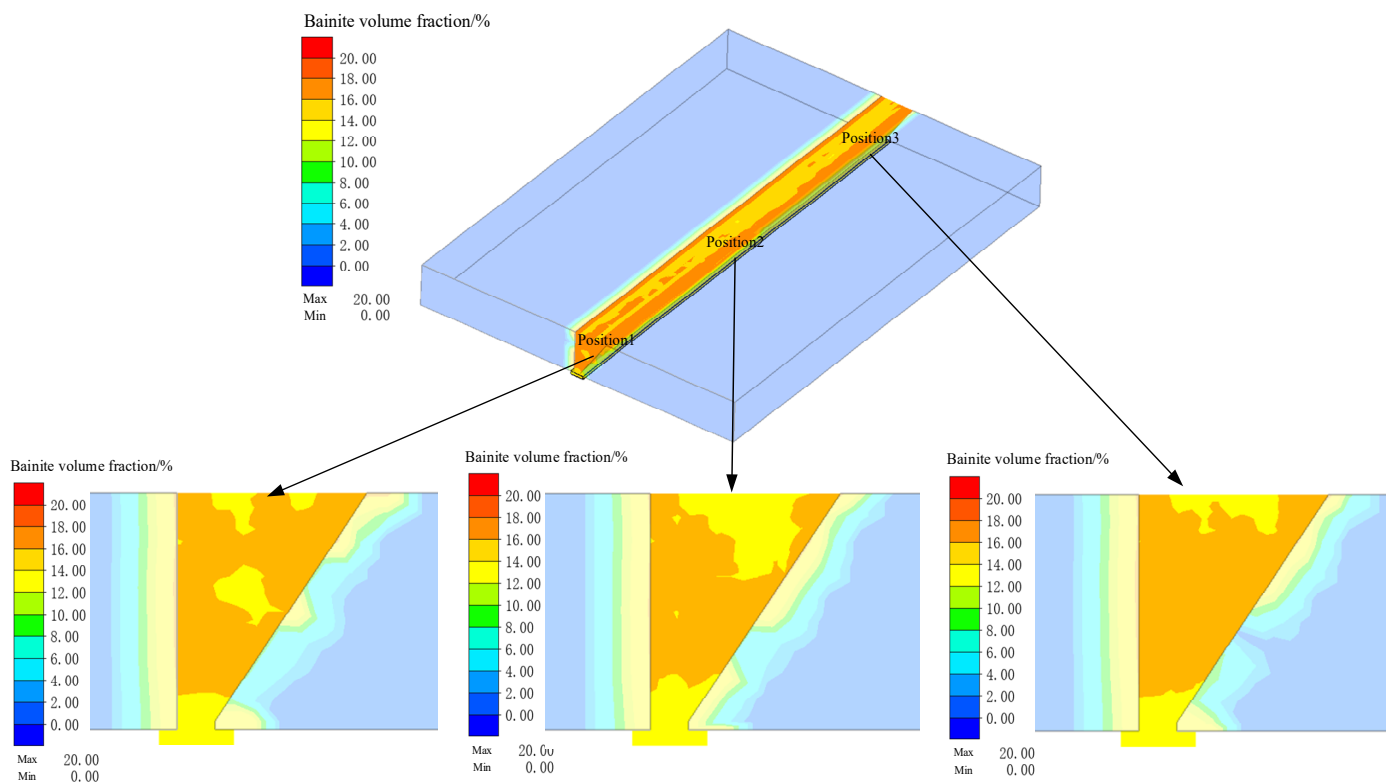

Fig. 12. Bainite volume fraction of different positions in the welds
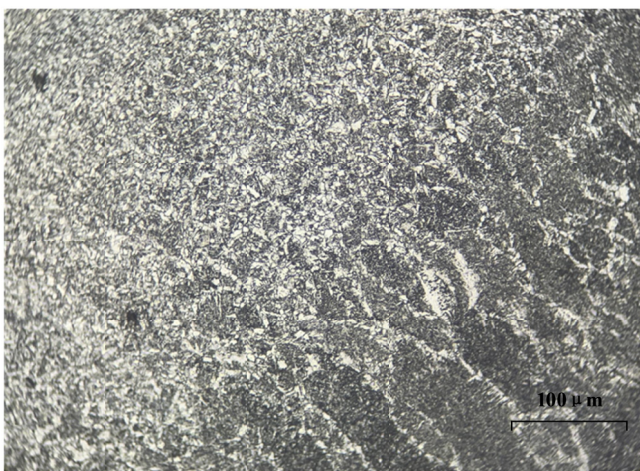

Fig. 13. Microstructure observation diagram of weld

ware – Simufact Welding, which can calculate the welding thermal cycle curve and welding temperature field cloud map of any unit node during the low temperature welding process.

(2) Based on the Kirkaldy phase transition model and the Koistinen-Marburger phase transition model, the equivalent display of the microstructure of the welding joint was successfully realized, and the different microstructure of each region was correlated with the $t_{8/5}$ cooling rate, moreover the largest bainite tissue content was found in the thermal influence area.

(3) The welding process parameters selected in low temperature welding test are verified by test and numerical simulation, which can provide reference for low temperature welding engineering of Q460GJCZ25 thick plate.

REFERENCES

[1] M. Yoshiki, T. Kanazawa, On the Mechanism of Propagation of Brittle Fracture in Mild Steel. J. Zosen Kiokai **1957** (102), 39-45 (2009). DOI: https://doi.org/10.2534/jjasnaoe1952.1957.102_39

[2] GB 50661-2011, Welding Code for Steel Structure (2021)

[3] A.K. Lakshminarayanan, V. Balasubramanian, Process parameters optimization for friction stir welding of RDE-40 aluminium alloy using Taguchi technique. T. Nonferr. Metal. Soc. **18** (3), 548-554 (2008). DOI: https://doi.org/10.1016/S1003-6326(08)60096-5

[4] J.A. Goldak, M. Akhlaghi, Computational welding mechanics. USA: Springer Verlag New York Inc **2005**, 59-63 (2005). DOI: https://doi.org/10.1007/b101137

[5] J. Goldak, A. Chakravarti, M Bibby, A new finite element model for welding heat sources. Metall. Trans. B **15** (2), 299-305 (1984). DOI: https://doi.org/10.1007/BF02667333

[6] M. Arunkumar, V. Dhinakaran, N.S. Shanmugam, Numerical prediction of temperature distribution and residual stresses on plasma arc welded thin titanium sheets. Int. J. Model. Simul. **41** (2), 146-162 (2019). DOI: https://doi.org/10.1080/02286203.2019.1700089

[7] D. Camilleri, P. Mollicone, T.G.F. Gray, Computational methods and experimental validation of welding distortion models. P. I. Mech. Eng. L-J. Mat. **221** (4), 235-249 (2007). DOI: https://doi.org/10.1243/14644207JMDA1

[8] M.A. Ezzat, A.S.E. Karamany, M.A. Fayik, Fractional order theory in thermoelastic solid with three-phase lag heat transfer. Arch. Appl. Mech. **82**, 557-572 (2012). DOI: https://doi.org/10.1007/s00419-011-0572-6

[9] C.G. De Andres, F.G. Caballero, C. Capdevila, et al., Application of dilatometric analysis to the study of solid-solid phase transformations in steels. Mater. Charact. **48** (1), 101-111 (2002). DOI:https://doi.org/10.1016/S1044-5803(02)00259-0

[10] Y. Ueda, J. Ronda, H. Murakawa, et al., Thermo-Mechanical-Metallurgical Model of Welded Steel: Part I: Evolution Equations for Internal Material Structures. Trans. JWRI **23** (2), 149-167 (1994). DOI: https://doi.org/10.18910/6090

[11] S. Ren, S. Li, Y. Wang, et al., Finite element analysis of residual stress in 2.25Cr-1Mo steel pipe during welding and heat treatment process. J. Manuf. Processes **47**, 110-118 (2019). DOI: https://doi.org/10.1016/j.jmapro.2019.09.019

[12] J.D. Robson, P. Upadhyay, A.P. Reynolds, Modelling microstructural evolution during multiple pass friction stir welding. Sci. Technol. Weld. Joi. 613-618 (2013). DOI: https://doi.org/10.1179/136217110X12813393169651

[13] H. Göhring, O. Fabrichnaya, A. Leineweber, et al., Thermodynamics of the Fe-N and Fe-N-C Systems: The Fe-N and Fe-N-C Phase Diagrams Revisited. Metall. Mater. Trans. **A 47**, 6173-6186 (2016). DOI: https://doi.org/10.1007/s11661-016-3731-0

[14] J.J. Cui, C.X. Lei, Z.W. Xing, et al., Predictions of the Mechanical Properties and Microstructure Evolution of High Strength Steel in Hot Stamping. J. Mater. Eng. Perform. **21**, 2244-2254 (2012). DOI: https://doi.org/10.1007/s11665-012-0180-9

[15] W. Ji, P. Zhang, K. Luo, Investigation of welding temperature field and residual stresses of corrugated steel web girders. Structures **44**, 1416-1428 (2022). DOI: https://doi.org/10.1016/j.istruc.2022.08.047

[16] L. Weingrill, M.B. Nasiri, N. Enzinger, Thermo-metallurgically coupled numerical simulation and validation of multi-layer gas metal arc welding of high strength pearlitic rails. Weld. World **63**, 63-73 (2019). DOI: https://doi.org/10.1007/s40194-018-0639-x

[17] S. Salimi, P. Bahemmat, M. Haghpanahi, A 3D transient analytical solution to the temperature field during dissimilar welding processes. Int. J. Mech. Sci. **79**, 66-74 (2014). DOI: https://doi.org/10.1016/j.ijmecsci.2013.11.015

[18] R. Hamilton, D. Mackenzie, H. Li, Multi-physics simulation of friction stir welding process. Eng. Computation. **27** (8), 967-985 (2020). DOI: https://doi.org/10.1108/02644401011082980

[19] A. Yazdipour, A. Heidarzadeh, Effect of friction stir welding on microstructure and mechanical properties of dissimilar Al 5083-H321 and 316L stainless steel alloy joints. J. Alloy. Compd. **680**, 595-603 (2016). DOI: https://doi.org/10.1016/j.jallcom.2016.03.307

[20] S. Jindal, R. Chhibber, N.P. Mehta, Effect of welding parameters on bead profile, microhardness and H 2 content in submerged arc welding of high-strength low-alloy steel. P. I. Mech. Eng. B-J. Eng. **228** (1), 82-94 (2014). DOI: https://doi.org/10.1177/0954405413495846

[21] Q. Sun, H.S. Di, J.C. Li, et al., A comparative study of the microstructure and properties of 800 MPa microalloyed C-Mn steel welded joints by laser and gas metal arc welding. Mater. Sci. Eng. A **669**, 150-158 (2016). DOI: https://doi.org/10.1016/j.msea.2016.05.079

[22] S.T. Mandziej, A. Vyrostkova. Creep and fracture behavior of long-annealed weld HAZ in CB2 steel. Weld. World, **64** (3), 573-590 (2020). DOI: https://doi.org/10.1007/s40194-020-00855-w

[23] J. Han, H.J. Li, Z.X. Zhu, et al., Microstructure and mechanical properties of friction stir welded 18Cr–2Mo ferritic stainless steel thick plate. Mater. Design **63**, 238-246 (2014). DOI: https://doi.org/10.1016/j.matdes.2014.05.070

[24] P.Y. Zhang, J. Zhang, B.Z. Li, Mechanical Properties and Microstructure Transformation Behavior for Welded Joints in Ship Plate Steel with High-Heat Input Welding. J. Mater. Eng. Perform. **31**, 944-952 (2021). DOI: https://doi.org/10.1007/s11665-021-06224-y